Experimental Observation of Convective Cell Formation due to a Fast Wave Antenna in the Large Plasma Device

M. J. Martin, W. Gekelman, B. Van Compernolle, P. Pribyl, and T. Carter

Department of Physics and Astronomy, University of California, Los Angeles, California 90095, USA

(Received 23 May 2017; published 17 November 2017)

An experiment in a linear device, the Large Plasma Device, is used to study sheaths caused by an actively powered radio frequency (rf) antenna. The rf antenna used in the experiment consists of a single current strap recessed inside a copper box enclosure without a Faraday screen. A large increase in the plasma potential was observed along magnetic field lines that connect to the antenna limiter. The electric field from the spatial variation of the rectified plasma potential generated $\vec{E} \times \vec{B}_0$ flows, often referred to as convective cells. The presence of the flows generated by these potentials is confirmed by Mach probes. The observed convective cell flows are seen to cause the plasma in front of the antenna to flow away and cause a density modification near the antenna edge. These can cause hot spots and damage to the antenna and can result in a decrease in the ion cyclotron range of frequencies antenna coupling.

Radio frequency (rf) plasma potential rectification is of general interest in commercial plasma processing reactors [1], broadcast antennas in the magnetosphere [2], and ion cyclotron resonance heating (ICRH) antennas in tokamaks [3]. ICRH will be an integral component for the international thermonuclear experimental reactor (ITER), where it is expected to couple up to 20 MW to the plasma [3]. In current ICRH tokamak experiments, a host of deleterious effects have been observed during antenna operation in the ion cyclotron range of frequencies (ICRF). These include an increase in the plasma ion impurity content [4,5], plasma facing components (PFCs) materials damage [6], modifications to the scrape-off layer (SOL) density profile [7,8], and ICRF power lost to the SOL [9,4]. The typically accepted cause of these problems is the dc rectification of the plasma potential, V_p [10]. These rectified potentials charge the plasma on background magnetic field $\vec{B}_0$ lines connected to or passing in front of antenna components. The spatial pattern of the rectified V_p produces dc electrostatic electric fields, $\vec{E}$, perpendicular to $\vec{B}_0$, which in turn lead to the formation of $\vec{E} \times \vec{B}_0$ convective cells that transport particles across the magnetic field [11].

To date, convective cells have only been measured partially and/or indirectly in fusion devices. In Alcator C-mod, emissive probes, ion sensitive probes, and gas puff imaging were used to indirectly measure 1D profiles of V_p and $\vec{E}$ [5,12]. In Tore Supra and ASDEX-Upgrade, reciprocating floating Langmuir probe and retarding field analyzer (RFA) measurements have measured cross-field floating potential and ion energy profiles [13–16]. These measurements, obtained with significant effort, rely on the alteration of the magnetic pitch angle through several discharges to build a 2D map of the potential structure field aligned to the antenna. In addition, use of the floating

potential may be misleading, as the floating and plasma potentials do not necessarily track each other and have different frequency response [17]. Though these measurements provide insight to the problem of convective cells and rf sheaths, plasma conditions change with varying magnetic pitch angle. An ideal measurement would be directly made across a SOL without adjusting the SOL plasma conditions.

In this Letter we report the first direct measurement of the convective cells using emissive and Mach probes over a two-dimensional locus in the vicinity of an ICRF antenna. The experiment is performed in the upgraded Large Plasma Device (LAPD) [18] at the Basic Plasma Science Facility (BAPSF) at the University of California, Los Angeles (UCLA). The LAPD plasma is housed in a cylindrical vacuum chamber that utilizes two independently operable cathode-anode discharge plasma sources to create a 19 m long, 60 cm diameter plasma column. A BaO cathode-anode discharge source is located at one end of the vessel and creates a 60 cm diameter plasma column ($n_e \sim 1 \times 10^{18}$ m^{-3}, $T_e \sim 4$ eV, $T_i = 1$ eV). A second plasma source comprising a 20 cm $\times$ 20 cm LaB$_6$ cathode-anode discharge is located at the opposite end of the chamber and creates a hotter, denser plasma (4×10^{18} m^{-3} < n_e < 8×10^{18} m^{-3}, $T_e \sim 10$ eV, $T_i = 1$ eV) on the machine axis. A schematic of the device is shown in Fig. 1(a). The plasma discharge typically lasts 10 ms and is repeated at a 1 Hz repetition rate.

This experiment is performed in a He plasma with an axial magnetic field of 1000 G along the z direction. The neutral He base pressure in the vacuum chamber is 1.7×10^{-4} Torr. The single current strap antenna used in the experiment includes elements common to tokamak ICRH antennas and is diagrammed in Fig. 1(b). All materials visible in the drawing are copper. The antenna is coaxially fed, with the center of the coax connected directly to the current strap (6 cm wide) and the outer
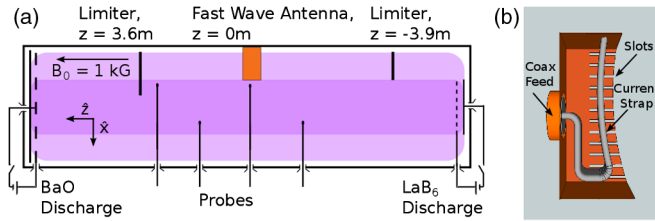
FIG. 1.   (a) A schematic of the experiment, not to scale. The coordinate system of the experiment is $z = 0$ at the fast wave antenna and $x = y = 0$ is along the LAPD axis. Two plasma sources are in operation during the experiment. The limiters block a direct connection between the antenna and the discharge circuitry along $\mathbf{B}_0$ field lines. (b) Diagram of the fast wave antenna with one wall of the enclosure removed. All conductors are copper, the coaxial antenna feed is shown on the center left, and the strap is visible within the box. The side slots are visible on the back wall of the enclosure.

conductor connected to the box enclosure (10 cm wide and 30 cm high). In these experiments the copper box enclosure is slotted so magnetic flux can penetrate the boundary. One side of the box is removed in Fig. 1(b) for clarity. On the interior of the box two insulating macor plates are epoxied to completely cover the slotted areas of the box in order to prevent a direct connection between the plasma and the current strap. There is no Faraday shield on the front face of this antenna for the present work. The antenna is inserted into the plasma column so that at $y = 0$ cm, its edge is located at $x = -10$ cm, corresponding to the edge of the high density plasma due to the LaB_6 discharge. Two conducting, grounded limiter plates, size 30.5 cm × 30.5 cm, are inserted on either side of the antenna, at $z = 3.6$ and $z = -3.9$ m and extend to $x \leq -9.9$ and $x \leq -4.5$ cm, respectively. The purpose of the limiters is to block a direct connection along $\vec{B}_0$ between the electrically floating cathode-anode systems on either end of the LAPD

and the single-strap antenna. In the private SOL created between the limiter located at $z = 3.6$ m and the antenna n_e varies from 10^{17}–10^{18} m^{-3} and T_e from 2–7 eV. These conditions are similar to those in tokamak SOL plasmas, e.g., Ref. [12]. The ion temperature during this experiment was measured spectrascopically using two different monochrometers looking at He II line (4685 Å). Both measurements yielded 1 eV ions with at least ½ eV uncertainty because the line is narrow. No ion heating was observed during the rf pulse.

During the experiment, the rf source energizes the antenna for ~2000 cycles with a frequency, $f_{rf} = 2.38$ MHz, and $f_{rf}/f_{ci} = 6.2$, where f_{ci} is the ion cyclotron frequency for singly ionized He. The rf source driving the antenna is a custom-built 150 kW push-pull rf amplifier [19]. The rf excitation in the antenna has a pronounced effect on the plasma potential. Plasma potential is measured with a floating emissive probe [20]. Before collecting emissive probe data the probe is moved to the center of the LAPD plasma column where the density is highest. Over successive plasma discharges the heating current is increased and the current-voltage characteristics of the probe are measured. Once the emission current is equal to the electron saturation current the heater settings are fixed and the sweeping circuitry is disconnected from the probe. The floating potential of the emissive probe is then recorded. Figure 2(a) shows a time trace of the antenna current and a time trace of the measured plasma potential at $x = -14$ and $y = -10$ cm. The dc plasma potential jumps by 80–96 V, which is large since the local electron temperature is on the order of 2.5 eV ($e\delta V_p/T_e \approx 30$). The spatial pattern of V_p is shown in Fig. 2(b) in an x-y plane at axial location $z = 65$ cm. The emissive probe accurately tracks the rf oscillation in the potential, but V_p shown in Fig. 2(b) has been digitally low-pass filtered to remove the oscillatory portion and obtain the average voltage. During the
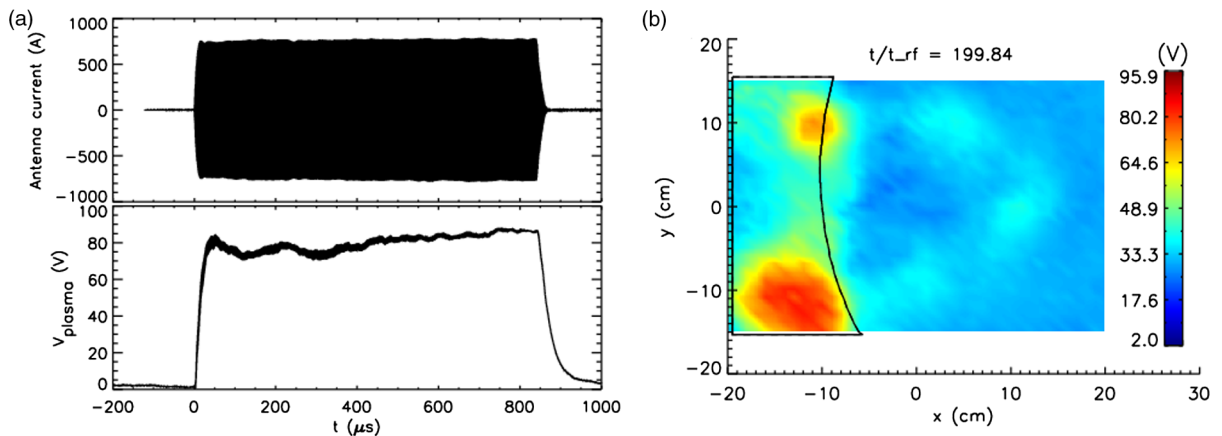

FIG. 2.   (a) Top panel: Time trace of the rf current on the antenna. Lower panel: representative time trace of plasma potential at $x = -14$, $y = -10$ cm. Potential increases of up to 90 V are observed after the antenna is powered up. (b) Plasma profile during the rf pulse taken at $z = 65$ cm. The outline of the antenna box is shown in solid lines. The locations of highest V_p are at the top and bottom of the ICRF antenna.

application of the rf pulse, the maximum plasma potential jumps to 96 V. The maximum change in the ion saturation current, $I_{\mathrm{isat}} \propto n\sqrt{T_e}$, signal is a factor of 1.6 during the rf pulse, which implies electron heating cannot explain the increase in V_p. Electron temperature measurements using a swept probe before and after the rf pulse show a small increase in T_e (2–3 eV) in front of the antenna and nowhere else. The potential in the interior of the plasma volume, i.e., on field lines that do not intersect the limiters or antenna, increases as well. This change in V_p on axis is the same as the change in the BaO and LaB$_6$ anode voltages during the rf pulse. The largest potentials are observed on field lines connected to the top and bottom of the antenna box. We estimate the emissive probe to be capable of tracking the rf oscillations in the plasma potential up to 10 MHz (based on probe impedance and the connection resistance determined from the slope of the swept probe characteristic), well above the 2.38 MHz operating frequency. In the areas with the most significant enhancement of the dc potential, the oscillation amplitude is no greater than 10 V. This indicates that the dc rectifying potential oscillation occurs not at the probe but much closer to the antenna in z or that some other mechanism is driving the potential rectification.

These results are consistent with antenna simulations performed for Tore Supra and ASDEX [21,22], in which the highest rf potentials similarly occur at the top and bottom of the antenna box. In antenna simulations, the quantity believed to be responsible for causing large dc potential drops between the plasma and the PFCs is the value of $\int \vec{E}_{\parallel}$ [21] or $\vec{E}_{\parallel}$ in front of the antenna [22]. Preliminary simulations using COMSOL of the rf antenna in the LAPD experiment show strongly enhanced $\vec{E}_{\parallel}$ fields near the top and the bottom of the box enclosure, giving credence to the conjecture that these are causing the large rectified sheaths.

The high dc potentials that form between the plasma and the grounded antenna produce ion acceleration into the antenna. Singly ionized Helium ions (He+) at 100 eV sputter copper with yields of 0.045 atoms/ion [23].

Evidence for sputtering was found during this experiment–probes that spent a substantial time in this plasma developed copper coatings, a phenomenon not observed during other experiments in the LAPD. Additionally, copper coating of the macor plates at the antenna were found after the experiment.

The spatial structure of V_p gives rise to electrostatic electric fields, $\vec{E} = \vec{\nabla} V_p$, which in turn generate $\vec{E} \times \vec{B}_0$ particle drifts. These drifts occur at a substantial fraction of the local ion sound speed, $c_s = \sqrt{[k_B(T_e + T_i)/m_i]}$, where T_e and T_i are the electron and ion temperatures, respectively, m_i the ion mass, and k_B is Boltzmann's constant. For the data shown in Fig. 3(a), the maximum flow speed at the bottom-right corner of the antenna is 0.67–0.84 c_s, assuming limits on the value of T_i are 5 or 1 eV, respectively. This is consistent with spectroscopically measured ion temperature values (1 eV) in the LAPD under similar conditions in other experiments. No change in the ion temperature (width of the HeII line at 4860 Å) was observed in this experiment. The experimental parameters were not favorable for ion heating. The vector plot in Fig. 3(a) shows the $\vec{E} \times \vec{B}_0$ motion derived from the steady-state V_p measurements. The color plot shows the magnitude of $\vec{E}$ in V/cm. The color bar also indicates the magnitude of the $\vec{E} \times \vec{B}_0$ drift in km/s. Convective cells can be observed on field lines connected to the top and bottom of the antenna, inside the private SOL created by the antenna and the limiter. Three much smaller vortices are also present in the bulk plasma. These are due to the background V_p profile and are not a direct consequence of the rf pulse on the antenna. The flow in the negative y direction during the rf pulse between $-10 \text{ cm} \leq \times \leq -5 \text{ cm}$ linking the two convective cells is due solely to the rf. The results discussed so far are computed from emissive probe measurements. Flow measurements were repeated with a six-faced Mach probe at the same axial location, and are shown in Fig. 3(b). The Mach probe results independently verify the presence of the convective cells measured by the emissive probe. The Mach probe consists of three orthogonal
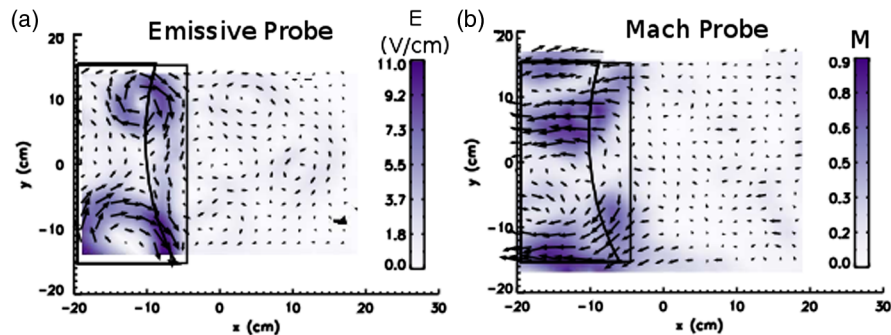

FIG. 3.   (a) The vectors show the $\vec{E} \times \vec{B}_0$ drifts calculated from V_p measurements using the emissive probe. The color shows the magnitude of the electrostatic electric field in V/cm. This is also the $\vec{E} \times \vec{B}_0$ flow speed in km/s ($\vec{B}_0 = 0.1$ T). (b) A vector field of the flow measured by the Mach probe. The color map shows the mach speed calculated from the measurements. The location of the antenna is shown on the left as well as the outline of the limiter at $z = 3.6$ m.

pairs of oppositely facing conducting tips, each independently biased to -150 V in order to collect I_{isat} The 1 mm Mach probe size was less than the 2 mm ion Larmour radius, marginally placing the Mach probe in the unmagnetized regime. The "unmagnetized" limit of Mach probe analysis was employed [24],

$$R = \frac{J^+_{isat}}{J^-_{isat}} = e^{\alpha \cdot v_f}, \qquad (1)$$

where $J^{\pm}_{isat}$ is the upstream or downstream ion saturation current density, v_f is the drift velocity normalized to $\sqrt{(k_B T_e/m_i)}$, and α is an order unity calibration factor. In this analysis, the value of α used was 1.3. The color map in Fig. 3(b) indicates the Mach number of the flow. Figure 3(b) shows similar features to Fig. 3(a). There are clear convective cells on field lines connected to the top and bottom of the antenna around $y = 10$ and $y = -10$ cm. In addition, there is a larger convective cell at the bottom. Missing are flow arrows connecting the two convective cells. This is likely due to the Mach probe being a less sensitive diagnostic than the emissive probe.

Convective cells are a cause for concern during ICRH in tokamaks because of a possible redistribution of the SOL density profile. In the present work this type of density modifications is estimated using the ion saturation current, $I_{isat} \propto n\sqrt{T_e}$. At the experimental rf power levels, no

significant change in T_e was measured, as determined by swept Langmuir probes consisting of a tantalum disk with alumina backing on one side and its exposed conductor facing the BaO plasma source. T_e values were obtained before the rf pulse and during 100 μs sweep periods starting 60 μs after the rf pulse. The difference between the two measurements is at most $\sim$3 eV, indicating low electron heating. Therefore, I_{isat} can be taken as a proxy for density. Figure 4 shows the evolution of the ion saturation current profiles, as five snapshots. Overplotted are vectors representing the $\vec{E} \times \vec{B}_0$ flow deduced from the plasma potential measurements, as in Fig. 3(a). Within 40 us after the antenna is powered up, the $\vec{E} \times \vec{B}_0$ flow pattern has established itself. At $t = 80$ μs, a substantial rearrangement of the ion saturation current profile took place in front of the antenna (near $x = -10$ cm). Decreases in I_{isat} are observed at the top, and increases near the bottom, consistent with the $\vec{E} \times \vec{B}_0$ flow pattern. At later times the profile recovers but remains displaced with respect to the pre-rf profile. After a few 100 μs the profile reaches a near-steady-state that lasts until the antenna is powered down. At that time the profile transitions back to the pre-rf profile. The dramatic transient modification in the first 100 μs is captured in the bottom right-hand panel. Displayed are time evolution of I_{isat} near $x = -9$ and $y = 0$ cm, for a range of antenna powers. At this location I_{isat} experiences a substantial decrease after the antenna is
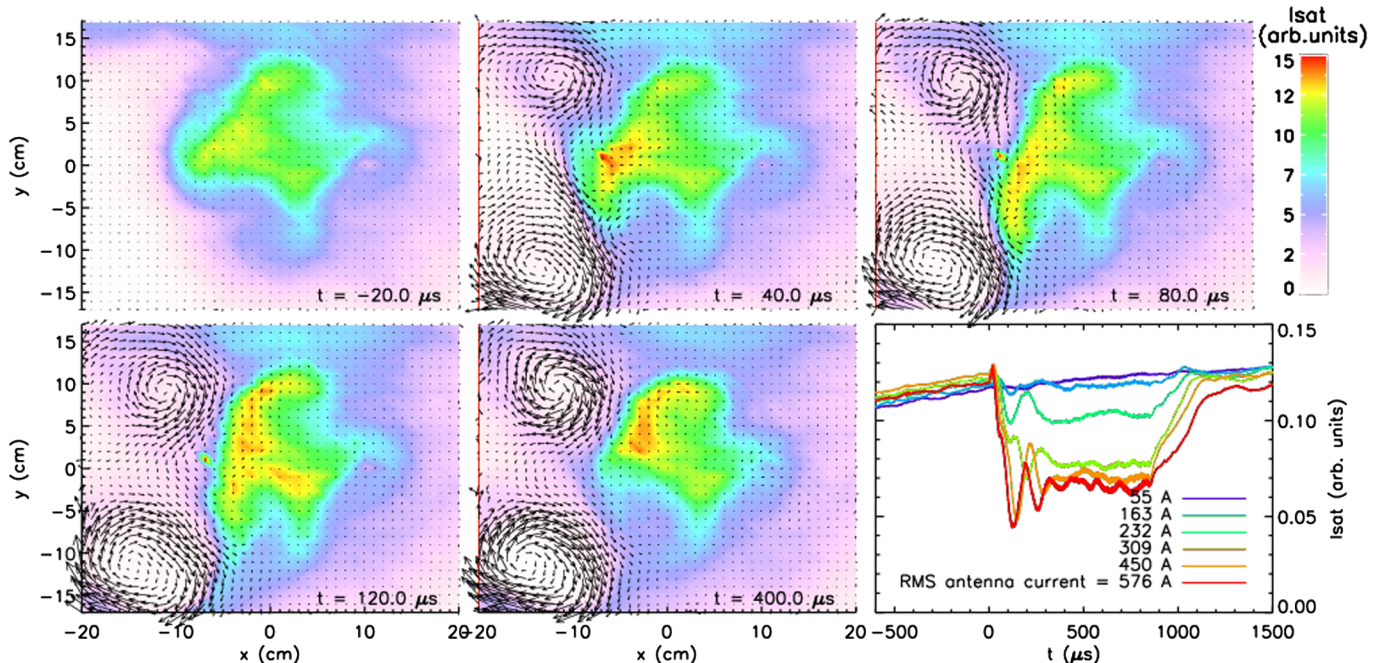

FIG. 4.   Five snapshots of the modification of the ion saturation current profile are shown. Substantial modifications are seen in front of the antenna with a decrease near the top and increase near the bottom, most dramatic at $t = 80$ us. The rf switches on at $t = 0$. Overplotted are vectors representing the $\vec{E} \times \vec{B}_0$ flow deduced from plasma potential measurements. The modifications of the profiles are consistent with the $\vec{E} \times \vec{B}_0$ flow patterns. Bottom right panel shows the time evolution of the ion saturation current near $x = -9$ and $y = 0$ cm as a function of antenna power, exhibiting a threshold at low powers and saturation at higher powers.

powered up at high antenna powers, with a 8 kHz transient oscillation, associated with the large profile modifications and subsequent relaxation as shown in the other panels of Fig. 4. The modification shows a clear threshold in power, with no observable changes at low powers. At higher powers saturation is observed with similar I_{isat} modifications even if the power is increased further. Similar results were obtained using lithium beam emission spectroscopy diagnostic in JET [25]. The results obtained here can be used as a benchmark for rf simulation codes which aim to incorporate density modifications and rf sheath effects.

Summary and conclusion.—Results on rf sheath rectification, convective cells, and density modification during fast wave launching are presented in unprecedented detail. The most significant V_p enhancements occur in the private SOL and are magnetically connected to the top and bottom of the antenna structure. This rf-enhanced potential caused observable sputtering and significant cross-field $\vec{E} \times \vec{B}_0$ flows in the SOL. Large scale density modifications were observed exhibiting decreases near the top of the antenna and increases near the bottom, consistent with the downward oriented flow at the front of the antenna due to the convective cells. Convection of SOL density could lead to high heat loads on antenna components, more pronounced in fusion devices than in LAPD. In this experiment, the density modifications display both a threshold at low powers and saturation at high antenna powers.

The data obtained in this experiment provide a valuable benchmark data set for the development of the next step rf simulation codes which aim to incorporate rf sheath effects and density modifications into the codes.

[1] M. A. Lieberman and A. J. Lichtenberg, *Principles of Plasma Discharges and Materials Processing* (John Wiley & Sons, Hoboken, NJ, 2005).

[2] J. Tu, P. Song, and B. W. Reinisch, J. Geophys. Res. **113**, A07223 (2008).

[3] J. R. Wilson and P. T. Bonoli, Phys. Plasmas **22**, 021801 (2015).

[4] M. Bures, J. J. Jacquinot, M. F. Stamp, D. D. R. Summers, D. F. H. Start, T. Wade, D. A. D'Ippolito, and J. R. Myra, Nucl. Fusion **32**, 1139 (1992).

[5] S. J. Wukitch, M. L. Garrett, R. Ochoukov, J. L. Terry, A. Hubbard, B. Labombard, C. Lau, Y. Lin, B. Lipschultz, D. Miller, M. L. Reinke, and D. Whyte (Alcator C-Mod Team), Phys. Plasmas **20**, 056117 (2013).

[6] P. Jacquet *et al.* (JET EFDA Contributors), Nucl. Fusion **51**, 103018 (2011).

[7] D. A. D'Ippolito, J. R. Myra, J. H. Rogers, K. W. Hill, J. C. Hosea, R. Majeski, G. Schilling, J. R. Wilson, G. R. Hanson, A. C. England, and J. B. Wilgen, Nucl. Fusion **38**, 1543 (1998).

[8] M. Bécoulet, L. Colas, S. Pécoul, J. Gunn, Ph. Ghendrih, A. Bécoulet, and S. Heuraux, Phys. Plasmas **9**, 2619 (2002).

[9] R. J. Perkins, J. C. Hosea, G. J. Kramer, J.-W. Ahn, R. E. Bell, A. Diallo, S. Gerhardt, T. K. Gray, D. L. Green, E. F. Jaeger, M. A. Jaworski, B. P. LeBlanc, A. McLean, R. Maingi, C. K. Phillips, L. Roquemore, P. M. Ryan, S. Sabbagh, G. Taylor, and J. R. Wilson, Phys. Rev. Lett. **109**, 045001 (2012).

[10] F. W. Perkins, Nucl. Fusion **29**, 583 (1989).

[11] D. A. D'Ippolito, J. R. Myra, J. Jacquinot, and M. Bures, Phys. Fluids B **5**, 3603 (1993).

[12] R. Ochoukov, D. G. Whyte, D. Brunner, D. A. D'Ippolito, B. LaBombard, B. Lipschultz, J. R. Myra, J. L. Terry, and S. J. Wukitch, Plasma Phys. Controlled Fusion **56**, 015004 (2014).

[13] L. Colas, J. P. Gunn, I. Nanobashvili, V. Petržílka, M. Goniche, A. Ekedahl, S. Heuraux, E. Joffrin, F. Saint-Laurent, C. Balorin, C. Lowry, and V. Basiuk, J. Nucl. Mater. **363–365**, 555 (2007).

[14] L. Colas, A. Argouarch, S. Brémond, M. Chantant, Y. Corre, M. Firdaouss, M. Goniche, D. Guilhem, J.-P. Gunn, J. Jacquot, M. Kubič, X. Litaudon, G. Lombard, O. Meyer, P. Mollard, and K. Vulliez, J. Nucl. Mater. **438**, S330 (2013).

[15] W. Zhang, Y. Feng, J.-M. Noterdame, V. Bobkov, L. Colas, D. Coster, T. Lunt, R. Bilato, J. Jacquot, R. Ochoukov, D. Van Eester, A. Křivská, P. Jacquet, and L. Guimarais (ASDEX-Upgrade Team), Plasma Phys. Controlled Fusion **58**, 095005 (2016).

[16] L. Colas, V. Bobkov, D. Carralero, M. Kočan, H. W. Müller, P. Manz, M. Kubič, J. P. Gunn, A. Herrmann, and V. Rohde (ASDEX-Upgrade Team), AIP Conf. Proc. **1580**, 259 (2014).

[17] N. Hershkowitz, in *Plasma Diagnostics* (Academic press, New York, 1989), Vol. 1, Chap. 3, p. 113.

[18] W. Gekelman, P. Pribyl, Z. Lucky, M. Drandell, D. Leneman, J. Maggs, S. Vincena, B. Van Compernolle, S. K. Tripathi, G. Morales, T. A. Carter, Y. Wang, and T. DeHaas, Rev. Sci. Instrum. **87**, 025105 (2016).

[19] M. J. Martin, P. Pribyl, W. Gekelman, and Z. Lucky, AIP Conf. Proc. **1689**, 070010 (2015).

[20] M. J. Martin, J. Bonde, W. Gekelman, and P. Pribyl, Rev. Sci. Instrum. **86**, 053507 (2015).

[21] L. Colas, S. Heuraux, S. Brémond, and G. Bosia, Nucl. Fusion **45**, 767 (2005).

[22] V. Bobkov *et al.* (ASDEX-Upgrade Team), Plasma Phys. Controlled Fusion **59**, 014022 (2017).

[23] D. Rosenberg and G. K. Wehner, J. Appl. Phys. **33**, 1842 (1962).

[24] I. H. Hutchinson, Plasma Phys. Controlled Fusion **44**, 1953 (2002).

[25] L. Colas, Ph. Jacquet, D. Van Eester, V. Bobkov, M. Brix, L. Meneses, P. Tamain, S. Marsen, C. Silva, D. Carralero, M. Kočan, H.-W. Müller, K. Crombé, A. Křivska, M. Goniche, E. Lerche, and F. G. Rimini (JET-EFDA Contributors, and ASDEX-Upgrade Team), J. Nucl. Mater. **463**, 735 (2015).